Article

Hydrogen diffusion and trapping in a cryogenic processed high-Cr ferrous alloy

Check for updates

Patricia Jovičević-Klug[1,2,4] ✉, J. Manoj Prabhakar [1,4], Cristiano Kasdorf Giesbrecht[1], Tim M. Schwarz[1], Carsten Bonnekoh[3], Michael Rieth[3] & Michael Rohwerder [1]

The effect of hydrogen diffusion and trapping was studied in a high-Cr ferrous alloy using an inverted scanning Kelvin probe and thermal desorption spectroscopy in correlation with microstructure and residual stress study. In addition, different processing of ferritic/martensitic 9Cr1WTaV alloy (EUROFER97) was tested in correlation with observed selected properties to observe induced changes in material degradation and surface. The activation energies for hydrogen traps were shown to have distinct peaks corresponding to different trapping mechanisms, including matrix dislocations and grain boundaries. For the cryogenically treated sample, an additional peak was also identified and correlated with increased carbide precipitation.

Materials used in the energy sector, especially those used in fusion, must be able to withstand high temperatures, high corrosive environments, high pressures, and high energy particle environments[1]. In addition, the operation of radioactive tritium is one of the main aspects of the future fusion energy sector. For this reason, the suppression of hydrogen (its isotope tritium) permeation in the first wall of fusion reactors is considered to be highly necessary and, at the same time, to minimize the loss of fuel[2–4]. In order to prevent hydrogen permeation, so called hydrogen permeation barriers are used in the form of coatings. Materials that can be used and are currently being tested as barriers on EUROFER; high-Cr steel, which will be used as a structural material in the first wall of A fusion reactor; are various oxides, nitrides, carbides, carbon, intermetallics, various metals such as tungsten and gold, and ceramic based barriers[4]. The challenge is not only the barrier but also to improve the substrate material (i.e., EUROFER97) in order to suppress hydrogen permeation and at the same time have superior properties (high corrosive and wear resistance, high toughness, high strength, etc.)[1–3,5–7].

Hydrogen permeation in ferrous alloys is considered to be a combined process of adsorption, dissociation, absorption, diffusion, and recombination coupled with desorption (Fig. 1). A hydrogen molecule (H_2) is adsorbed on the surface of the barrier and dissociates into hydrogen atoms (shown in Fig. 1 as H in a bubble). The adsorbed H atoms then diffuse from the surface into the barrier and move toward the interface of the substrate, in this case, EUROFER97. The hydrogen barrier should effectively prevent the adsorption of H_2 molecules and dissociation into atomic H and/or H atoms from diffusing into the EUROFER97. However, H atoms can also diffuse

further into the EUROFER97, and recombination into molecular H_2 and desorption can occur[4].

Important factors that influence hydrogen permeation are dislocations (Fig. 1 point e), grain boundaries (Fig. 1 point d), vacancies (Fig. 1 point f), traps (Fig. 1 points b and c), impurities (intermetallics formed with alloying atoms (Fig. 1 point a), beside Fe in the EUROFER97), chemical composition and microstructure. All these factors act as hydrogen traps and can potentially modify the behavior of the hydrogen. The trapping of free hydrogen atoms occurs only if the potential energy of hydrogen atoms is lowered in these trapping sites[2–4,7–9].

As stated by many researchers in the fusion community, including from one of the last reviews on the given topic by Rieth et al.[1]. the exploration of hydrogen effect on production and interaction with ferrous alloys (especially EUROFER97) used in the fusion sector has not yet been explored well, and there are many questions left unanswered. One of the ways to tailor the microstructure while providing modified properties and surface modification of ferrous alloys is a novel processing technique of ferrous alloys called cryogenic processing (CP)[10]. CP is a type of processing in which a material is subjected to cryogenic temperatures to tailor the preferred microstructure to achieve the desired properties of the material. CP is a specialized technique that treats both the surface and bulk of the material at the same time and is a cost-effective, low-emission and sustainable technique that challenges many of the known techniques[10–14]. Only a few studies have been carried out on the application of CP in high-Cr ferrous alloys[15,16], which have shown that CP has great potential, but there is a lack of studies on the application of CP in EUROFER97.

[1]Max Planck Institute for Sustainable Materials (Max-Planck-Institut für Eisenforschung GmbH), Max-Planck-Straße 1, 40237 Düsseldorf, Germany. [2]Alexander von Humboldt Postdoc Research Fellow, Alexander von Humboldt Foundation, Jean-Paul-Straße 12, 53173 Bonn, Germany. [3]Institute for Applied Materials, Karlsruhe Institute of Technology, Hermann-von-Helmholtz-Platz 1, 76344 Eggenstein-Leopoldshafen, Germany. [4]These authors contributed equally: Patricia Jovičević-Klug, J. Manoj Prabhakar. ✉e-mail: p.jovicevic-klug@mpie.de
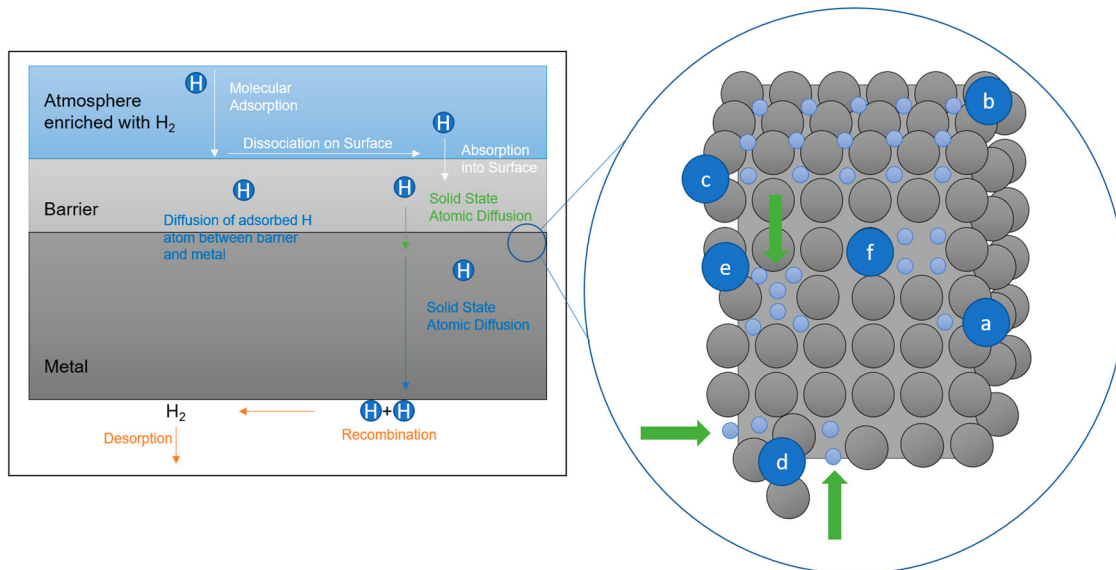
Fig. 1 | Schematic representation of hydrogen permeation from hydrogen enriched atmosphere through barrier to the EUROFER97 adapted from figures by Rönnebro et al.[4] and Pundt and Kirchheim 2006[41]; Li et al.[42]. The factors indicated on the figure influence hydrogen permeation. These factors are impurities (point **a**), traps (points **b** and **c**), grain boundaries (point **d**), dislocations (point **e**) and vacancies (point **f**).

In this study, hydrogen permeation studies are combined with microstructure analysis and residual stress measurements to understand hydrogen diffusion and trapping behavior of the high-Cr ferrous alloy 9Cr1WTaV alloy (EUROFER97). The amount of trapped hydrogen calculated from the hydrogen permeation measurements is compared with the results from thermal desorption spectroscopy. Furthermore, this study compares conventional processing with cryogenic processing (the same material, just different thermal processing) in order to provide insight and a possible new technique for providing a hydrogen permeation barrier for materials used in the fusion energy sector, but also for hydrogen production, storage, and delivery sectors.

Microstructure and residual stress analysis

The results of the microstructure analysis are shown in Fig. 2a–d. Chemical composition[17] and heat treatment of each group is described in chapter "Methods under Material, processing, microstructure and phase analysis". Group marked C-EF is the conventional and control group, while group T-EF is the test and CP group. A detailed microstructural analysis is performed in our previous study by Jovičević-Klug et al.[5], of which only the most relevant microstructure for our testing is summarized and presented in this section.

Both tested groups show martensite as the main phase in the matrix. Martensitic laths can be observed to be finer in CP test-EF compared to C-EF by 30–40%, depending on the location of the observation. A smaller amount of retained austenite (RA) was detected in the T-EF group (below 0.1 vol%), whereas around 1 vol% in the control group C-EF[5]. This was also confirmed by XRD analysis, which was done along with a detailed microstructural analysis in our previous study by Jovičević-Klug et al.[5]. The detailed analysis of the previous study also showed that the matrix of both samples is mainly composed of Fe, Ni, and some Cr. In addition to martensite and RA, remnants of the sigma phase were also detected in the TEM[5]. In both the samples, different precipitates in the form of carbides/carbonitrides and Ce-oxides were present. The types of carbides, which are present in both samples are M_7C_3 (enriched with Cr and Fe), M_3C_2 (enriched with Cr and Fe), M_6C (enriched with Cr, Fe, and W), $M_{23}C_6$ (enriched with Cr and Fe), MC (enriched with Ta) and MCN (enriched with V only or V and Ta), this is based on an in-depth study by XRD, SEM, ESBD, TEM and APT analysis[5] (selected carbides can also be observed in Fig. 2). The precipitation of carbides and carbonitrides occurs mainly at prior austenitic grain boundaries (PAG), which can be nicely seen in Fig. 2. However, some precipitation of microscopic carbides, mainly enriched with Cr and nanoscopic $M_{23}C_6$ is also occurring within martensitic laths (Fig. 2a–c). The main difference, apart from the higher conversion of RA into martensite, is also the increased precipitation of MC, M_7C_3, and $M_{23}C_6$ carbides of 63%, 53%, and 62%, respectively, in the phases after the application of CP on EUROFER97[5]).

Cerium oxides are also present which were added for easier manufacturability of the selected alloy and to remove excess oxygen or sulfur during manufacturing, as its binding capacity is greater than other elements[18]. In addition, the role of Ce and La (which is also present in Ce core and shell-oxide as observed by APT) is also to do refinement of the steel during solidification[18,19]. Therefore, Ce-oxides, which are also observed in this alloy, also have a higher rare earth elements (REEs) content. However, the presence of REEs can only be detected within the oxides and not in the matrix or precipitates, this means oxide act as isolated system (Fig. 2a–d). The APT measurement of the matrix (Supplementary Fig. 1) showed no signals of REEs in the mass spectrum, confirming this statement. The composition of the alloy based on the APT analysis shows for the matrix 90.11 at% Fe, 8.44 at% Cr, 0.28 at% W, 0.10 at% V and the remaining amount consists of impurities of Si, Al, Mn, Co, and Ni. The EDS and APT analyses showed that the composition of Ce-oxide is on average 20.69 ± 2.54 at%, 11.41 ± 2.31 at% Ta, 40.64 ± 10.31 at% N, 0.18 ± 0.91 at% Al, 30.32 ± 10.12 at% O, 1.57 ± 0.32 at% Nd, 0.31 ± 0.36 at% La and 0.35 ± 0.12 at% Mg (Fig. 2c, d), depending on the position (shell/core). It is important to note that the enrichment of specific elements within Ce-oxides is divided into the core and shell of the oxide, which can be seen in the SEM images and APT measurements in Fig. 2d. This confirms that Ce-oxides act effectively as removers of oxides and agglomerates of REEs.

To correlate the microstructure changes between two different processing routes (conventional and CP) with the dimensional stability of the crystal lattice, residual stress measurements were done (Fig. 3b). Our results showed that the results are similar for both samples (C-EF and T-EF) for directions of 0° (C-EF = −311 ± 32 and T-EF = −292 ± 19) and 45° (C-EF = −296 ± 18 and T-EF = −294 ± 14). However, the main difference is in the direction of 90° (C-EF = −251 ± 25 and T-EF = −313 ± 26), where the difference is 24%, where the C-EF sample treated with CP shows lower values compared to T-EF, which shows that in the direction of 90°, CP promotes the build-up of more compressive stresses and release tensile
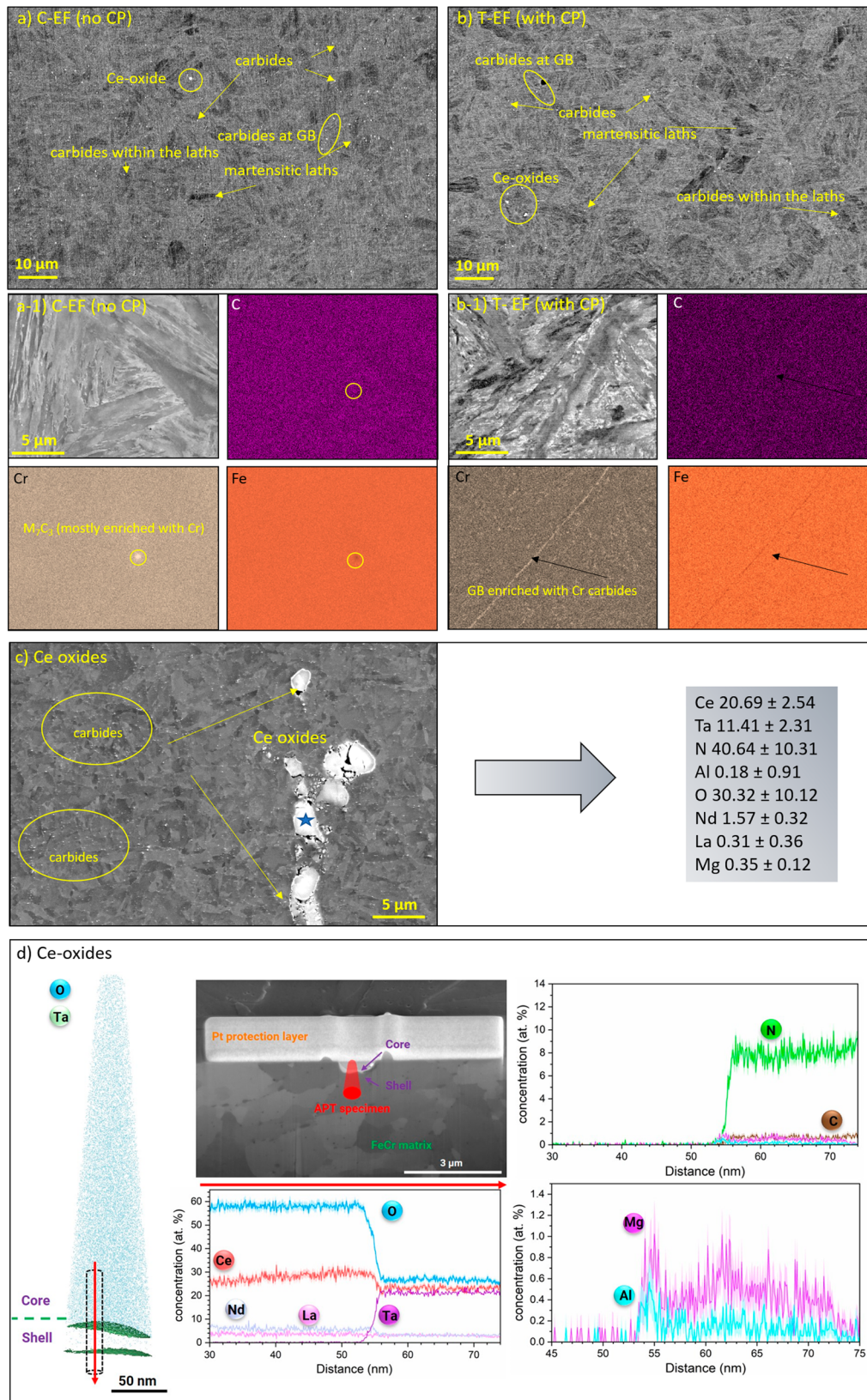
Fig. 2 | Microstructure analysis of both groups of the samples C-EF control-EF group and test-EF (with CP) group. a (a-1), **b** (b-1) Micrographs of samples for C-EF and T-EF, respectively, whereas a-1 and b-1 are figures with higher magnification in order to show martensitic laths and precipitation of selected carbides. **c** Ce- oxides presence in the alloy, which can be observed as isolated agglomerations. **d** Ce-core-shell oxide structure was analyzed by atom probe tomography (APT) to investigate the enrichment and separation of REEs.

Fig. 3 | Residual stress measurements of T-EF (test group with CP) and C-EF (control group no CP) samples of high-Cr ferrous alloy (EUROFER97).
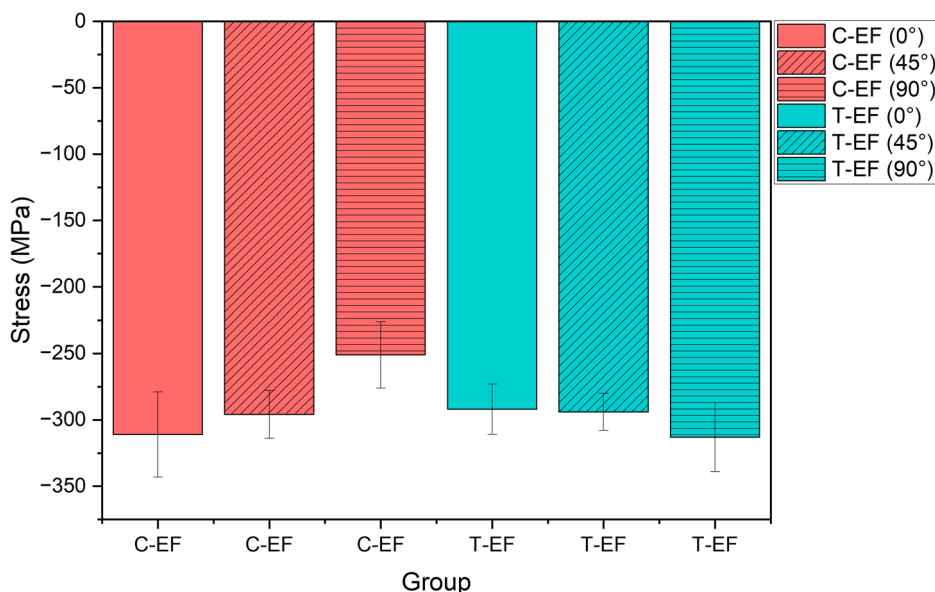
stresses compared to the control, C-EF sample. This observation can be related to the increased transformation of RA into martensite and the increased precipitation of finer carbides during CP, which changes the dimensional stability of the martensitic matrix and causes crystal defects. This is an important observation as the preferred direction is at 90°, and the permeation of hydrogen atoms will be along this direction, which can then influence the hydrogen permeation kinetics.

Hydrogen permeation

The hydrogen permeation measurements were carried out using the KP-based potentiometric method[20–23]. In this technique, the entry side of the sample is in contact with the electrolyte, facilitating the electrochemical charging of hydrogen into the material. As hydrogen atoms migrate through the sample to the detection side, they are absorbed by the Pd film, a process facilitated by the low chemical potential of Pd for hydrogen. Upon contact with the Pd surface, the formation of a hydrogen electrode (shown in Eq. 1) is observed, even under a dry nitrogen atmosphere, due to a nanoscopic layer of water[20,21].

$$H_{ab} \rightarrow H_{ad}^{+} + e_{Pd}^{-} \tag{1}$$

This interaction leads to a reduction in work function, resulting in a notable decrease in the electrode potentials recorded by the KP. Unlike the conventional Devanathan–Stachurski (DS) technique for hydrogen permeation[24,25], which measures the hydrogen oxidation current, the Kelvin probe (KP) technique quantifies the hydrogen electrode potential in a dry nitrogen atmosphere. The hydrogen exit side of the sample in the KP-based technique is exposed to a dry nitrogen atmosphere, unlike the oxidizing electrolyte conditions in the DS technique, which requires special treatments and precautions[26]. The hydrogen permeation current density values were also previously found similar to those obtained from the standard DS technique[27].

The dissolution of H in Pd (α-Pd) proceeds until reaching a critical concentration, beyond which the β-Pd hydride phase begins to form. This transition occurs at approximately 2.4 at% of H in Pd at room temperature. Exceeding this concentration threshold, the α and β phases coexist over a broad compositional range, stabilizing the concentration of H dissolved in Pd. This stabilization effect is directly reflected in the potential measurements obtained via the KP, demonstrating the pinning of the potentials. The potential corresponding to the hydrogen electrode formed by the adsorbed H on the surface of Pd and the absorbed H in the Pd follows the Nernst

equation (Eq. 2) and depends linearly on the concentration of the hydrogen in Pd ($c_{H^{Pd}}$)[22,27]:

$$E = E_{SHE}^{*} + m \ln(c_{H}^{Pd}) \tag{2}$$

The slope (m) in the aforementioned equation is determined to be 130 mV per decade[22,27], a characteristic attributed to the nanocrystalline structure of the Pd deposited on the surface. With the potential at the commencement of the binary phase ($c_{H}^{Pd} = 2.4$ at%) normalized to 0 V, these parameters allow for the transformation of the potentials obtained at different times derived from the KP into a concentration of H in Pd (c_{H}^{Pd}) vs time (t) representation.

To examine the diffusivity of hydrogen in the sample while excluding the effects of the trapped hydrogen, it is crucial to implement a two-step permeation measurement. This approach involves initially saturating the traps during the first step, followed by an exclusive analysis of lattice diffusivity in the second step[28,29]. In the current study, the initial step is conducted at a lower cathodic potential. Subsequently, the cathodic potential is shifted to a more negative value (thereby increasing hydrogen activity at the entry side) prior to the potential stabilization induced by the onset of the β-Pd hydride phase. This potential shift for the two-step measurement in both the C-EF and T-EF samples is depicted by the red curves in Fig. 4a, b, respectively. The potentials recorded by the Kelvin probe (KP) during these measurements are represented by the black curves. It is evident that for both samples, the shift in the applied potentials led to a modification in the rate of change of surface potentials recorded by the KP, observable within minutes following the altering of the applied potential.

Figure 5 presents the evolution of hydrogen concentration in palladium, derived from the electrochemical potential versus time data depicted in Fig. 4. The curve can be segmented into three distinct phases. Initially, the hydrogen concentration in palladium remains negligible during the trap-filling phase until all available traps are occupied. Calculated from the final linear segments from the second step in Fig. 5, the permeation current density values for the C-EF and T-EF samples are 1.05 μA/cm² and 1.62 μA/cm², respectively. Similarly, the total time lags (t_{lag}) for these samples, determined by extending the linear segments from the first step to intersect with the x-axis in Fig. 5, are 320 min and 262 min, respectively. It should be noted that the total time lag (t_{lag}) derived from the curves comprises both the duration required to saturate the traps and the time for lattice diffusion. To
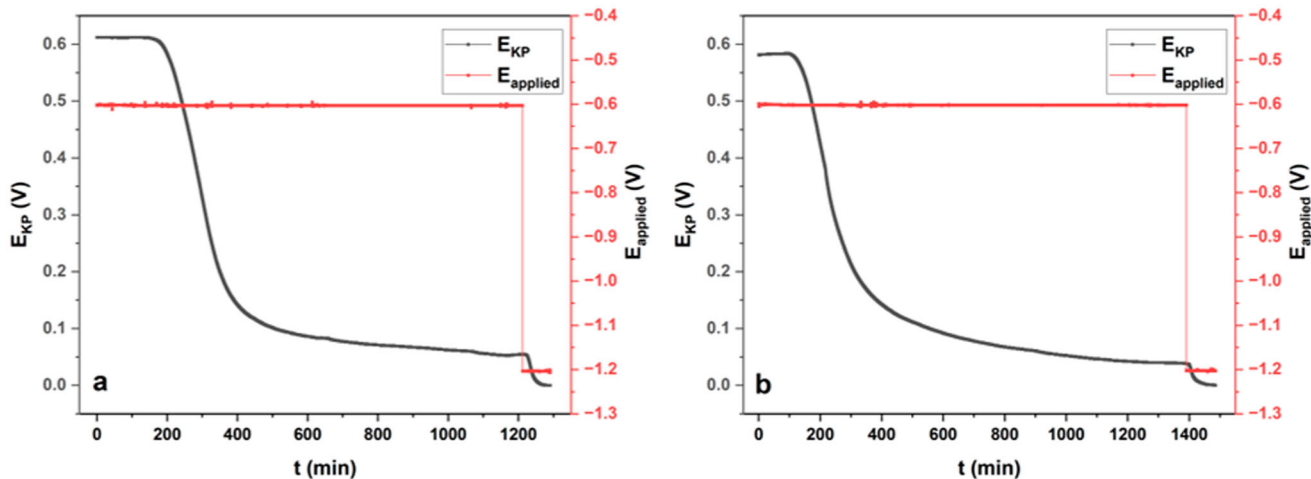
Fig. 4 | The evolution of the surface potentials with time measured by KP (black) and the applied potentials (red). a represents the results for the control sample C-EF and **b** represents the results for the test sample T-EF sample.
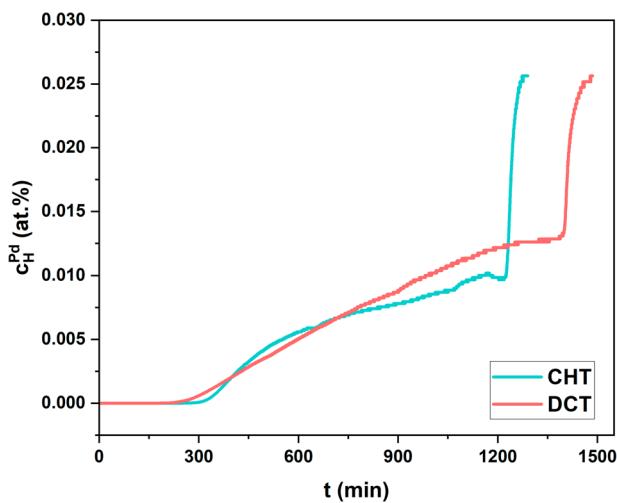

Fig. 5 | Permeation curves showing the concentration of hydrogen in the palladium layer (c_H^{Pd}) as a function of time for the C-EF and T-EF samples.

isolate the time lag associated exclusively with lattice diffusion (t_L)—which is obtained during the second phase at elevated activity following trap saturation at a lower activity—the time at which the activity was increased to the second step should be deducted from the time obtained from the intersection of the linear section in the second step with the x-axis. Consequently, the values of t_L for the C-EF and T-EF samples are determined to be 15 min and 10 min, respectively. Utilizing these values, the lattice diffusivity values can be computed using the formula applicable under potentiostatic polarization conditions (Eq. 3)[27,30]:

$$D = \frac{L^2}{6t_L} \qquad (3)$$

The diffusivity values determined for the C-EF and T-EF samples are 6.89×10^{-7} cm²/s and 10.33×10^{-7} cm²/s, respectively, with the T-EF sample exhibiting a marginally higher diffusivity. Similarly, the permeation current density is also slightly higher in the T-EF sample. Hence, CP effectively leads to a structure that is more conducive to hydrogen permeation, rather than acting as a barrier. These observations can be attributed to the reduced presence of RA in the sample that underwent CP. Previous studies employing the DS technique have explored how an increased amount of RA

within the matrix leads to a reduction in effective diffusivity[7,31,32]. This effect is due to the increase in the diffusion path (length), or increased tortuosity, for hydrogen diffusion and the interface between the matrix and RA, which serves as traps for hydrogen. The microstructural changes resulted in decreased tortuosity for permeation of hydrogen after CP, therefore resulting in higher diffusivity and permeation current density in the T-EF sample.

Hydrogen trapping

Figure 6a, b illustrate the hydrogen desorption spectra, which vary with temperature at different heating rates (ϕ) for the C-EF and T-EF samples, respectively. These spectra were modeled using Gaussian peaks (as shown in Supplementary Figs. 2 and 3), from which the peak temperatures (T) were determined. The activation energies for the traps were calculated using Kissinger analysis, which involves plotting $\ln(\phi/T^2)$ against $1/T$ and deriving the activation energies from the slope of these plots. The Kissinger plots for the C-EF and T-EF samples are presented in Supplementary Figs. 4 and 5, respectively. While the spectra for the C-EF samples could be accurately modeled with 2 peaks, the spectra for the T-EF samples required 3 peaks for a precise fit.

The first peak observed in the C-EF sample (as shown in Supplementary Fig. 2) and the second peak in the T-EF sample (Supplementary Fig. 3), both with an activation energy of approximately 35 kJ/mol, are attributed to hydrogen trapping by dislocations within the martensite matrix[33,34]. The subsequent peak in the C-EF sample and the third peak in the T-EF sample, which exhibit lower binding energy in the range of approximately 26–33 kJ/mol, is likely due to the grain boundaries between RA and the martensite matrix[34,35]. Additionally, the extra peak in the T-EF sample, characterized by a higher binding energy of about 47 kJ/mol, could result from the increased presence of carbide precipitates in the samples that underwent CP[36]. The phenomenon of lower binding energy traps resulting in peaks at higher temperatures was observed previously in martensitic steels[37].

The total amount of desorbed hydrogen from all the traps in the C-EF and T-EF samples are 2.4 ± 0.4 ppm and 2.4 ± 0.2 ppm, respectively. The marginally higher number of traps in the C-EF sample from the desorption measurements correlates well with the increased time-lag or reduced diffusivity in this sample from the hydrogen permeation measurements. The TDS results are also in agreement with the microstructural changes and stress relief observed after the CP treatment, resulting in a structure conducive to the permeation of hydrogen and reduced trapping sites.

The conclusions of this study are not only important and associated with the energy sector, but also for hydrogen production, storage and delivery sectors. The results of this study also highlight
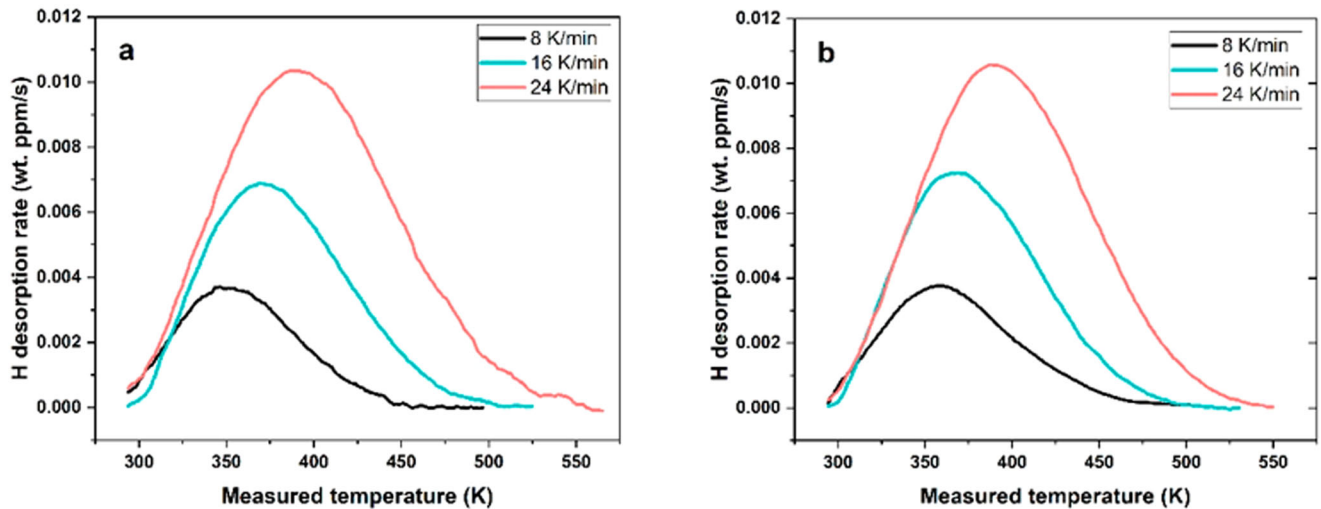
Fig. 6 | Hydrogen desorption rates during TDS measurements, where the black line represents a desorption rate of 8 K/min, the blue line represents 16 K/min and the red line represents 24 K/min. a shows TDS results for control sample C-EF and **b** shows TDS results for test sample T-EF.

the influence of cryogenic processing (CP) on the microstructure, residual stresses, and hydrogen permeation behavior of high-Cr steels (including EUROFER97), which can be summarized as follows: (1) both C-EF and T-EF samples, mainly consist of a martensitic matrix. The martensitic laths in the CP T-EF sample are 30–40% finer compared to the C-EF counterpart. Increased precipitation of MC, M_7C3, and $M_{23}C_6$ carbides by 63%, 53%, and 62%, respectively, was observed in the CP-treated group, mainly at prior austenitic grain (PAG) boundaries and within martensitic laths. (2) Similar residual stress values were observed for both samples in the 0° and 45° directions. However, a significant difference was observed in the 90° direction, indicating that CP promotes higher compressive stresses associated with increased transformation of RA to martensite and finer carbide precipitation. (3) Employing the KP-based potentiometric method, it was found that the T-EF sample exhibits slightly higher diffusivity and permeation current density, suggesting that CP results in a structure more permeable to hydrogen. (4) Activation energies for hydrogen traps were determined, with distinct peaks corresponding to different trapping mechanisms, including dislocations in the martensite matrix and grain boundaries between retained austenite and martensite. An additional peak in the T-EF sample indicates increased carbide precipitation from CP.

Methods
Material, processing, microstructure, and phase analysis
EUROFER97 is a Cr-rich iron alloy (chemical composition in wt%: 0.11 C, 0.4 Mn, 9 Cr, 0.12 Ta, 1.1 W, 0.03 N, 0.15 V, base Fe, others <0.012), was supplied by the Karlsruhe Institute of Technology (KIT), Germany[17]. The EUROFER97 samples were divided into two sub-groups, C-EF (control and conventionally heat treated) and T-EF (tested and CP treated), where the temperature of austenitization was Ta = 1273 K/0.5 h and quenching rate (1073–723 K) ~ 10 K/s, afterwards C-EF was subjected to 1 cycle of tempering at 823 K for 2 h, whereas the other subgroup T-EF was subjected to CP for 24 h at 77 K. After CP T-EF group has undergone 1 cycle of tempering at the same conditions as C-EF. The samples were heat treated at the Max Planck Institute for Sustainable Materials GmbH (MPI SusMat), Germany. Both sub-groups were heat treated in an Ar atmosphere under a high vacuum. This was done to eliminate the influence of N_2 gas on the microstructure during hardening and tempering. Samples were metallographically prepared for further analysis, according to Jovičević-Klug et al.[38] for the preparation of cryogenically treated ferrous alloys. Microstructural analysis of EUROFER97 alloy was performed using a scanning electron microscope (SEM) Zeiss Crossbeam 550 FIB-SEM Merlin II at MPIE, Germany.
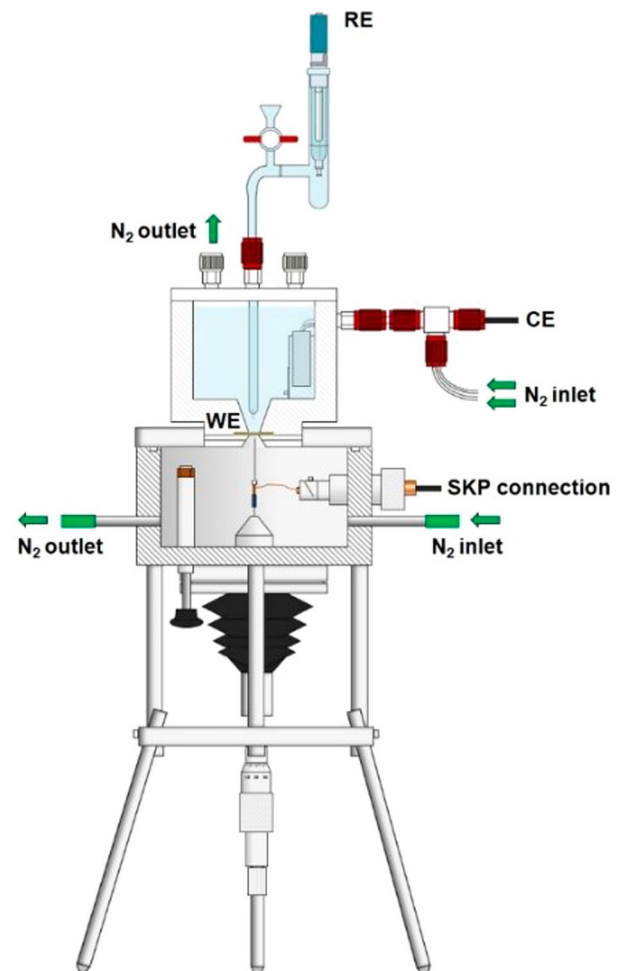

Fig. 7 | Schematic of the custom-built inverted Kelvin probe setup.

Atom probe tomography
APT samples were prepared using a Ga-FIB (Helios 5 CX) following the standard sample preparation protocol described in Thompson et al.[39]. APT experiments were performed using a Cameca LEAP 5000 series (Reflector (XR)) atom probe. A reflector instrument was used to obtain a higher mass
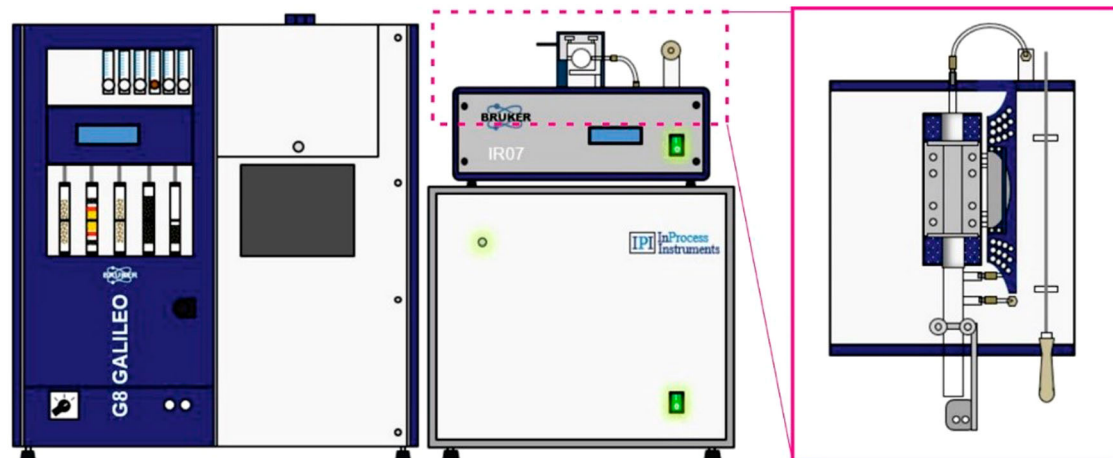
Fig. 8 | Thermal desorption spectroscopy setup showing the top view of the infrared furnace (inset) and the mass spectrometer connected to the G8 Galileo system.

resolution to distinguish the different signals expected from different RE elements and their oxides. The APT measurement was performed in laser pulse mode with a laser energy of 20–40 pJ and a repetition rate of 100 kHz at a base sample temperature of 40 K with an average detection rate of 1.0 ion per 100 pulses. Data reconstruction was performed using Cameca's Integrated Visualization and Analysis Software (IVAS) in AP Suite 6.3.

Residual stress measurements
The residual stress measurements were carried out using a Rigaku SmartLab having a Cu Kα rotating anode X-ray source. The diffractometer is equipped with a micro area beam optic (500 μm by 500 μm beam size), a 5-circle goniometer, and a HyPix3000 area detector. For each sample a residual stress measurement was done for the major phases (weight fraction > 10%). The 2Θ position of a reflex selected for the respective phase was measured for 13 different sample tilts ($-63.5° \geq chi \geq +63.5°$), for three different stress directions (PHI = 0°, PHI = 45° and PHI = 90°) each. The 2Θ position is used to calculate the residual stress according to the $\sin^2\psi$-method[40].

Hydrogen permeation with an inverted Kelvin probe
Measurements of hydrogen permeation were conducted utilizing a custom-built inverted Kelvin probe (KP) apparatus, as depicted in Fig. 7. The material under investigation, referred to as the working electrode (WE) in Fig. 7, was positioned between an electrochemical cell constructed from PTFE on the upper side and the Kelvin probe chamber on the lower side. The hydrogen-entry side of the sample is the side facing the Teflon cell, which was filled with an electrolyte solution composed of 0.1 M H_2SO_4 and 20 mg/L thiourea. The thiourea acts as a recombination inhibitor and promotes the uptake of hydrogen into the sample.

A platinum (Pt) foil, 25 μm in thickness and 99.99% pure, obtained from Goodfellow GmbH and a commercial silver/silver chloride (Ag/AgCl) electrode (containing 3 mol/L KCl) sourced from Metrohm, served as the counter electrode (CE) and reference electrode (RE), respectively, as indicated in Fig. 7. The sample's exit side, which faces the KP chamber, was coated with a 100 nm layer of palladium (Pd) using a Leybold Univex 450 physical vapor deposition system, and the KP chamber was maintained under a dry nitrogen atmosphere. Hydrogen introduction on the entry side was performed via potentiostatic polarization at various potentials, and the in-situ changes in electrode potential of the Pd surface during this process were recorded using the KP.

Thermal desorption spectroscopy (TDS)
Hydrogen was introduced into the samples measuring $10 \times 15 \times 1$ mm^3 electrochemically using a three-electrode setup. This process involved applying a voltage of -1.2 V for one hour in an aqueous solution of 0.1 M

H_2SO_4 with 20 mg/L NH_4SCN, a similar solution used for hydrogen permeation studies described in the previous section. Hydrogen detection was carried out by gradually increasing the temperature in an infrared furnace from 298 K to 1173 K, utilizing a mass spectrometer connected to a G8 GALILEO system from Bruker. The hydrogen detection measurements were started immediately after charging the samples. The setup with a top view of the infrared furnace is shown in Fig. 8. The experiments were conducted at various heating rates (ϕ) ~ 8 K/min, 16 K/min, and 24 K/min, to determine the activation energy of hydrogen desorption from different traps.

Data availability
The raw and processed data required to reproduce these findings are available from the corresponding author upon request.

References
1. Rieth, M. et al. Impact of materials technology on the breeding blanket design—recent progress and case studies in materials technology. *Fusion Eng. Des.* **166**, 112275 (2021).
2. Engels, J., Houben, A. & Linsmeier, C. Hydrogen isotope permeation through yttria coatings on Eurofer in the diffusion limited regime. *Int. J. Hydrog. Energy* **46**, 13142–13149 (2021).
3. Yaktiti, A., Dreano, A., Carton, J. F. & Christien, F. Hydrogen diffusion and trapping in a steel containing porosities. *Corros. Sci.* **199**, 110208 (2022).
4. Rönnebro, E. C. E., Oelrich, R. L. & Gates, R. O. Recent advances and prospects in design of hydrogen permeation barrier materials for energy applications—a review. *Molecules* **27**, 6528 (2022).
5. Jovičević-Klug, P. et al. Designing advanced high-Cr ferrous alloys for next-generation energy applications through cryogenic processing. *Appl. Surf. Sci.* **665**, 160290 (2024).
6. Rieth, M. et al. Technological processes for steel applications in nuclear fusion. *Appl. Sci.* **11**, 11653 (2021).
7. Garcia, D. C. S., Carvalho, R. N., Lins, V. F. C., Rezende, D. M. & Dos Santos, D. S. Influence of microstructure in the hydrogen permeation in martensitic-ferritic stainless steel. *Int. J. Hydrog. Energy* **40**, 17102–17109 (2015).
8. Wipf, H. Solubility and-diffusion of hydrogen in pure metals and alloys. *Phys. Scr.* **94**, 43–51 (2001).
9. Yagodzinskyy, Y. et al. Hydrogen effects on tensile properties of EUROFER 97 and ODS-EUROFER steels. *J. Nucl. Mater.* **444**, 435–440 (2014).

10. Jovičević-Klug, P. & Rohwerder, M. Sustainable new technology for the improvement of metallic materials for future energy applications. *Coat* **13**, 1822 (2023).

11. Toth, L. Cryogenic treatment against retained austenite. in *Mérnöki Szimpózium a Bánkiban* 181–186 (Obuda University, Budapest, Hungary, 2021).

12. Senthilkumar, D. Deep cryogenic treatment of En 31 and En 8 steel for the development of wear resistance. *Adv. Mater. Process. Technol*. **8**, 1769–1776 (2021).

13. Kara, F. & Takmaz, A. Optimization of cryogenic treatment effects on the surface roughness of cutting tools. *Mater. Test.* **61**, 1101–1104 (2019).

14. Jovičević-Klug, P. et al. Austenite reversion suppression with deep cryogenic treatment: a novel pathway towards 3rd generation advanced high-strength steels. *Mater. Sci. Eng.* **873**, 145033 (2023).

15. Jovičević-Klug, P., Jovičević-Klug, M., Sever, T., Feizpour, D. & Podgornik, B. Impact of steel type, composition and heat treatment parameters on effectiveness of deep cryogenic treatment. *J. Mater. Res. Technol.* **14**, 1007–1020 (2021).

16. Jovičević-Klug, P. et al. Assessment of deep cryogenic heat-treatment impact on the microstructure and surface chemistry of austenitic stainless steel. *Surf. Interfaces.* **35**, 102456 (2022).

17. Materna-Morris, E. et al. *Final Report on the EFDA Task Structural Material Eurofer97-2, Characterization of Rod and Plate Material: Structural, Tensile, Charpy, and Creep Properties*. (2007).

18. Adabavazeh, Z., Hwang, W. S. & Su, Y. H. Effect of adding cerium on microstructure and morphology of Ce-based inclusions formed in low-carbon steel. *Sci. Rep.* **7**, 1–10 (2017).

19. Ji, Y., Zhang, M. X. & Ren, H. Roles of lanthanum and cerium in grain refinement of steels during solidification. *Metals* **8**, 884 (2018).

20. Senöz, C., Evers, S., Stratmann, M. & Rohwerder, M. Scanning Kelvin Probe as a highly sensitive tool for detecting hydrogen permeation with high local resolution. *Electrochem. Commun.* **13**, 1542–1545 (2011).

21. Evers, S. & Rohwerder, M. The hydrogen electrode in the "dry": a Kelvin probe approach to measuring hydrogen in metals. *Electrochem. Commun.* **24**, 85–88 (2012).

22. Evers, S., Senöz, C. & Rohwerder, M. Hydrogen detection in metals: a review and introduction of a Kelvin probe approach. *Sci. Technol. Adv. Mater.* **14**, 14201–14213 (2013).

23. Schaller, R. F. & Scully, J. R. Measurement of effective hydrogen diffusivity using the Scanning Kelvin Probe. *Electrochem. Commun.* **40**, 42–44 (2014).

24. Devanathan, M. A. V. & Stachurski, Z. The adsorption and diffusion of electrolytic hydrogen in palladium. *Proc. R. Soc. Lond. A Math. Phys. Sci.* **270**, 90–102 (1962).

25. Devanathan, M. A. V. & Stachurski, Z. The mechanism of hydrogen evolution on iron in acid solutions by determination of permeation rates. *J. Electrochem. Soc.* **111**, 619 (1964).

26. Manolatos, P., Jerome, M. & Galland, J. Necessity of a palladium coating to ensure hydrogen oxidation during electrochemical permeation measurements on iron. *Electrochim. Acta* **40**, 867–871 (1995).

27. Wu, C. H., Krieger, W. & Rohwerder, M. On the robustness of the Kelvin probe based potentiometric hydrogen electrode method and its application in characterizing effective hydrogen activity in metal: 5 wt. % Ni cold-rolled ferritic steel as an example. *Sci. Technol. Adv. Mater.* **20**, 1073–1089 (2019).

28. McBreen, J., Nonis, L. & Beck, W. A method for determination of the permeation rate of hydrogen through metal membranes. *J. Electrochem. Soc.* **113**, 1218 (1966).

29. Manolatos, P., Le, C. J., Duret-Thual, C. & Jérome, M. Use of pure metals to analyse hydrogen electrochemical permeation in steels. *Le. J. Phys. IV* **05**, C7–409 (1995).

30. Zakroczymski, T. Adaptation of the electrochemical permeation technique for studying entry, transport and trapping of hydrogen in metals. *Electrochim. Acta* **51**, 2261–2266 (2006).

31. Chan, S. L. I., Lee, H. L. & Yang, J. R. Effect of retained austenite on the hydrogen content and effective diffusivity of martensitic structure. *Metall. Trans. A Phys. Metall. Mater. Sci.* **22**, 2579–2586 (1991).

32. Olden, V., Thaulow, C. & Johnsen, R. Modelling of hydrogen diffusion and hydrogen induced cracking in supermartensitic and duplex stainless steels. *Mater. Des.* **29**, 1934–1948 (2008).

33. Wei, F. G. & Tsuzaki, K. Response of hydrogen trapping capability to microstructural change in tempered Fe–0.2C martensite. *Scr. Mater.* **52**, 467–472 (2005).

34. Saito, K. & Takai, K. Hydrogen desorption behavior trapped in various microstructures of high-strength steels using thermal desorption analysis. *Met. Mater. Trans. A Phys. Met. Mater. Sci.* **52**, 531–543 (2021).

35. Barrera, O. et al. Understanding and mitigating hydrogen embrittlement of steels: a review of experimental, modelling and design progress from atomistic to continuum. *J. Mater. Sci.* **53**, 6251–6290 (2018).

36. Depover, T. & Verbeken, K. Hydrogen trapping and hydrogen induced mechanical degradation in lab cast Fe-C-Cr alloys. *Mater. Sci. Eng.: A* **669**, 134–149 (2016).

37. Frappart, S. et al. Hydrogen trapping in martensitic steel investigated using electrochemical permeation and thermal desorption spectroscopy. *Scr. Mater.* **65**, 859–862 (2011).

38. Jovičević-Klug, P., Lipovšek, N., Jovičević-Klug, M. & Podgornik, B. Optimized preparation of deep cryogenic treated steel and Al-alloy samples for optimal microstructure imaging results. *Mater. Today Commun.* **27**, 102211 (2021).

39. Thompson, K. et al. In situ site-specific specimen preparation for atom probe tomography. *Ultramicroscopy* **107**, 131–139 (2007).

40. Hauk, S. *Structural and Residual Stress Analysis by Nondestructive Methods*. (Elsevier, Amsterdam, the Netherlands, 1997).

41. Pundt, A. & Kirchheim, R. Hydrogen in metals: microstructural aspects. *Annu Rev. Mater. Res.* **36**, 555–608 (2006).

42. Li, X. et al. Review of hydrogen embrittlement in metals: hydrogen diffusion, hydrogen characterization, hydrogen embrittlement mechanism and prevention. *Acta Metall. Sin.* **33**, 759–773 (2020).

Acknowledgements

Author contributions

Patricia Jovičević-Klug: Conceptualization, Methodology, Validation, Formal Analysis, Investigation, Writing-original draft, Writing-review & editing, Visualization, Funding acquisition. J. Manoj Prabhakar: Methodology, Formal Analysis, Writing-original draft, Writing-review & editing, Visualization. Cristiano Kasdorf Giesbrecht: Visualization, Writing-original draft, Writing-review & editing. Tim M. Schwarz: Methodology, Formal Analysis, Writing-original draft, Writing-review & editing. Carsten Bonnekoh Writing-review & editing, Resources. Michael Rieth: Writing-review & editing, Resources, Supervision. Michael Rohwerder: Writing-review & editing, Resources, Supervision.

Funding

Competing interests

The authors declare no competing interests.

Additional information

Supplementary information The online version contains supplementary material available at
https://doi.org/10.1038/s41529-024-00522-1.

Correspondence and requests for materials should be addressed to Patricia Jovičević-Klug.

Reprints and permissions information is available at
http://www.nature.com/reprints

Publisher's note Springer Nature remains neutral with regard to jurisdictional claims in published maps and institutional affiliations.